Optimizing a low-energy electron diffraction spin-polarization analyzer for imaging of magnetic surface structures

Robert Frömter,[1,a)] Sebastian Hankemeier,[1] Hans Peter Oepen,[1] and Jürgen Kirschner[2]
[1]*Institut für Angewandte Physik, Universität Hamburg, Jungiusstr. 11, 20355 Hamburg, Germany*
[2]*Max-Planck-Institut für Mikrostrukturphysik, Weinberg 2, 06120 Halle, Germany*

(Received 12 July 2010; accepted 12 December 2010; published online 2 March 2011)

A newly designed scanning electron microscope with polarization analysis (SEMPA or spin-SEM) for the acquisition of magnetic images is presented. Core component is the spin detector, based on the scattering of low-energy electrons at a W(100) surface in ultrahigh vacuum. The instrument has been optimized with respect to ease of handling and efficiency. The operation and performance of a general low-energy electron diffraction (LEED) detector for SEMPA have been modeled in order to find the optimum operating parameters and to predict the obtainable image asymmetry. Based on the energy dependence of the secondary electron polarization and intensity, the detector output is simulated. For our instrument with optimized performance we demonstrate experimentally 8.6% polarization asymmetry in the domain structure of an iron whisker. This corresponds to 17.2% image contrast, in excellent agreement with the predicted simulated value. A contrast to noise ratio of 27 is achieved at 5 ms acquisition time per pixel. © *2011 American Institute of Physics*. [doi:10.1063/1.3534832]

I. INTRODUCTION

For more than 20 years, the scanning electron microscope with polarization analysis (SEMPA or spin-SEM) has been used to study magnetic patterns at surfaces, in ultrathin films, and in nanostructures. During that period it has proven its potential to address various topics, e.g., the magnetic structure of domain walls,[1,2] ultrathin films,[3] exchange coupled films,[4] antiferromagnetically coupled oxides,[5] and the spin-reorientation transition.[6] Recently, special attention has been paid to widen the range of application of spin-SEM by utilizing various techniques for surface preparation, like dusting[7] or sputtering. Meanwhile, procedures have been established that make the investigation of nearly all kind of material and sample feasible, and spin-SEM has developed to a standard technique for the investigation of magnetic structures in the range from several microns down to 5 nm.[8]

The unique feature of the technique is that the magnetization orientation is directly measured. This can be achieved by detecting the spin polarization of the secondary electrons (SE), which are antiparallelly aligned to the magnetization. Hence, utilizing SEMPA means to create secondaries point by point and analyze the electrons with respect to their spin polarization, i.e., combining a SEM and a polarization detector in one instrument. To achieve optimal performance, the conditions dictated by the physical process of spin polarized secondary electron emission have to be considered. To obtain best results, both components, SEM column and spin detector have to be optimized. In this paper, we report on the design of a polarization detector optimized for the use in a spin-SEM. This detector is designed and already used in combination with a new SEM column that is as well optimized for the application in a SEMPA.[9]

Worldwide, three different types of detectors are used in spin-SEMs for polarization analysis, i.e., the Mott,[10] low-energy diffuse scattering (LEDS),[11] and low-energy electron diffraction (LEED) (Refs. 12–14) detectors. The Mott detector is based on the scattering of high-energy electrons at atom cores, while the low-energy detectors utilize the multiple scattering of electrons at surfaces of a single crystal (LEED) or at amorphous films (LEDS). Common to all these detectors is a low efficiency in the range of 2×10^{-4} or less.[15] The up to 2 orders of magnitude more efficient exchange-based detectors, Fe(001)-$p(1\times1)$O (Ref. 16) and Co/W(110),[17] require two successive measurements for each component of spin polarization and they rely on scattering of electrons with a narrow energy distribution. Their advantage in efficiency would be completely lost in SEMPA application as the energy spread is disjunctive to that of the SE. Thus, low efficiency is the crucial point that makes the optimizing of the instruments in all respects necessary. Due to our continuous experience with LEED detectors, we have explored the possibility to optimize the performance of this detector with respect to its application for SEMPA.

The paper is organized as follows. In the first paragraph, we introduce our new spin-SEM system and the realization of a new LEED detector. In the following paragraph, we work out theoretically the optimized performance of a detector when LEED at W(001) is utilized in the SEMPA application. From these considerations, certain design criteria follow, which are discussed in the third paragraph. Finally, the performance of our new detector design is compared with the results from the modeling.

II. EXPERIMENTAL SETUP

The microscope is set up in an ultrahigh vacuum (UHV) chamber, which can be baked to at least 150 °C and is operated at 5×10^{-11} mbar residual gas pressure. Under these

a)Electronic mail: rfroemte@physik.uni-hamburg.de. Fax: +49 (40) 42838-6368. Tel.: +49 (40) 42838-3312.

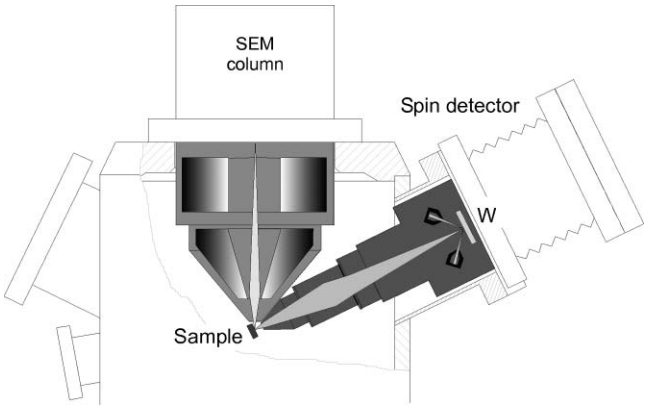

FIG. 1. Arrangement of column, sample, and spin detector within the UHV chamber. Both, the SEM and the retractable detector operate at a working distance of 8 mm. Since the detector is oriented in normal take-off geometry to maximize sensitivity, the SEM is scanning at 64° tilt angle with respect to the sample surface. The sample is mounted on a five-axis goniometer stage (not shown). The interior of column and detector schematically indicates the primary and secondary electron beams, together with one scattering plane of the W-crystal and two electron counters for the (2,0) beams (not to scale).

conditions, the magnetic contrast from an iron sample has proven to be largely preserved for several days. Samples can be quickly inserted into the microscopy chamber by means of a load lock and can be transferred into a directly attached preparation chamber under UHV conditions.

One design criterion has been to achieve as much flexibility as possible for applying the high-resolving electron beam from the SEM column. For that purpose, several UHV ports have been oriented with straight view onto the sample. On such flanges, there are mounted the spin analyzer, an Ar-ion sputter gun, a hemispherical energy analyzer for Auger electron analysis, and an electron beam evaporator for iron film deposition. In order to achieve high detection efficiency, it is important to keep the distance sample/spin-detector optics small. Thus, to maintain unhindered sample access for the other devices, the spin detector can be retracted.

A. Geometric design considerations

The important issue for an optimized spin-SEM is to maximize the angular acceptance of the polarization analyzer. For that reason, normal take-off geometry was chosen. Additionally, the distance between sample and detector optics was minimized. The two conditions put strong limitations on the geometrical arrangement. The angle between SEM column and detector optics should be much smaller than 90° to maintain an acceptable sample tilt with respect to the column axis. Too large angles will cause a serious deterioration of lateral resolution in the tilt direction. Too small angles will strongly reduce the size of the extraction optics cross section. The final solution is illustrated in Fig. 1: Straight access to the sample at a collection distance of 8 mm (to front end of detector) is possible at a sample tilt of 64° for a conical extractor optics with full opening angle of 49°. In this geometry, a SEM working distance of 8 mm is feasible.

The objective lens of the SEM is responsible for a magnetic stray field along the optical axis, which decreases with increasing working distance. An additional shielding reduces the stray field to 250 μT at the sample under typical working conditions (7 kV). A precessional rotation of the measured spin-polarization vector has not been observed within an error margin of 1°. This most advantageous result is due to the fast acceleration of the electrons toward the spin detector by the first elements of the optics. The electric field of the SEM column at the sample surface is quite small and is easily overcome by the potential gradient of 56 V mm^{-1} from the first acceleration lens of the transfer optics, which has been calculated including the outer ground shield. The effects of the column's electrostatic and magnetic stray fields on the SE trajectories are compensated by the beam steering elements (quadrupole deflectors) of the detector optics.

B. Spin detector

The detector for the spin-SEM is displayed in Fig. 2. Scattering at the W(001) surface is performed at normal incidence. For that geometry, at a kinetic scattering energy of $E_0 = 104.5$ eV, the (2,0) LEED beams appear at a fixed angle of $\vartheta_0 = 40.64°$ [see Eq. (9)] with respect to the surface plane. To preserve the propagation direction of the scattered electrons, the crystal as well as its complete surroundings including the drift tube and lens 6 are held at the same potential, termed scattering potential U_s. The (2,0) beams can leave the field-free region around the W(001) crystal through four grids fixed at U_s, which separate the scattering from the counting section. A second set of grids, mounted right behind, are set to a potential close to sample ground and, therefore, act

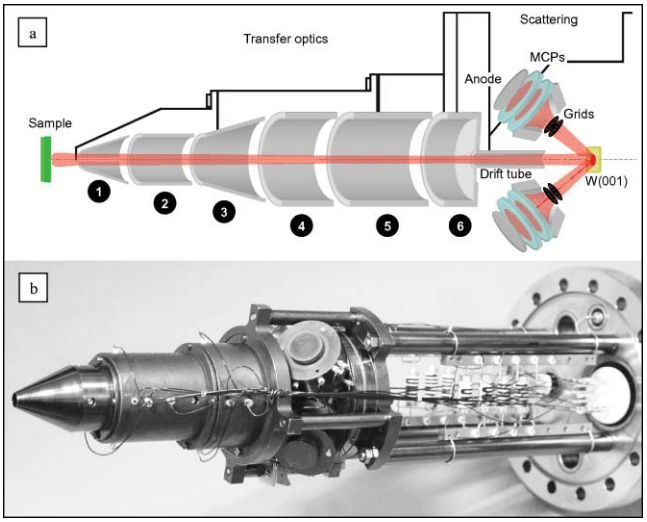

FIG. 2. (Color online) (a) Schematic of the spin detector. The transfer optics consist of a series of electrostatic tube lenses labeled 1–6 and a drift tube to define the beam divergence. Lenses 1 and 4 have been doubly split to form quadrupoles for beam steering. After scattering at the W crystal, the elastically scattered electrons that form the four (2,0) beams are first filtered by a retarding grid and amplified by a double MCP setup. The resulting current pulses on the four anodes can then be recorded by external electronics. A photograph of the entire spin detector with cabling is shown in part (b). The transfer optics on the left are followed by the scattering section in the center of the image. Adjacent is the voltage divider network for supplying the MCP stacks. It is suspended between the standoffs that mount the detector onto the DN100 ConFlat base flange containing all required electrical feedthroughs.

as high-energy pass filter. These retarding grids are used to block all SE generated at the W crystal and to suppress part of the inelastically scattered electrons. After passing both grids, an elastically scattered electron is accelerated into a dual microchannel plate (MCP) assembly for current pulse generation. Between the retarding grid and the MCP entrance, a tapered optical element is mounted. With this electrode, the electron beam is defocused before hitting the front of the first channel plate. Due to the defocusing, the whole plate area can be illuminated by the electrons. This is important to increase the expected lifetime, i.e., to increase the total number of detected events before the MCP quality degrades. In addition, the lower area intensity reduces the dead time of the plate assembly, as subsequent electrons will not hit exactly the same microchannel. The current pulses generated in the MCP stack are collected with an anode plate and, after high-voltage decoupling, fed into counting electronics.

To clean the W(001) surface, the single crystal can be flash heated above 2000 K from its rear by electron bombardment from a hot filament. Within 30 s after flashing, the detector is ready again for measuring. The whole cycle requires less than a minute.

As will be discussed in the following paragraphs, the SE emission is characterized by a wide energy spread with varying polarization and an emission into half space. To fulfill the conditions for optimized spin-detector performance (small angle/energy spread) would imply, however, that only a small fraction of the total SE emission could be utilized for spin analysis. Hence, the spin-polarization analyzer in a spin-SEM has to work at less favorable conditions in order to cover a large part of the SE spectrum. The goal is to find the optimum in the antagonism of degrading polarization sensitivity versus increasing count rates upon increase of the angle and energy acceptance. From general considerations about the SE emission, it was deduced that the detector with best performance (for spin-SEM application) should accept all the SE up to at least 10 eV, while the acceptance angle of the detector should be as large as possible.[18] The solution for the latter requirement is to put the sample into the focal plane of the detector system. By this, a large emission angle is transformed into a quasiparallel beam configuration. This means that the majority of all the electrons transferred into the detector are scattered at conditions close to normal incidence. In our design (see Fig. 2), there is a drift tube at the end of the optics, which is essential for adjusting the beam.The drift tube allows tuning of the electrons into a parallel beam configuration just by maximizing the sum of the four scattered intensities. The tube permits only electron beams with an angular spread of at maximum $\pm 5^\circ$ to be transmitted.

Electrons with different energies are scattered into different angles. Hence, LEED with fixed exit apertures gives a discrimination of energy in itself via the limitation of the angular spread of the scattered beams. In our setup, the grid support mounts act as such apertures (Fig. 2). For idealized normal incidence conditions, these apertures define an energy spread of roughly $\pm$ 10 eV around the nominal scattering energy. Details will be discussed later on.

The first two lens elements of the transfer optics in front of the detector are set to high potential (2–3 kV) to accelerate as many SE as possible into the optics. The first and fourth lens elements have been split into four segments each, so they can act as beam steering elements (electrostatic quadrupoles). They correct for angular deviations due to electrostatic and magnetic fields of the SEM column and sample tilt. The main effect of the first quadrupole is to center the field of view of the detector with respect to the SEM scan area, while the second quadrupole adjusts the LEED pattern with respect to the MCP entrance apertures by minimizing the experimental asymmetry.

C. SEM column

The UHV version of the Zeiss Gemini system is used in our microscope. This column was designed as primary source for scanning Auger microscopy and SEMPA**.** It is equipped with a Schottky field emission cathode and a combined electromagnetic/electrostatic objective lens. The electron-optical properties are superior to conventional microscopes, as the column combines high current with high spatial resolution, even at relatively low primary-beam energies. It, thus, fits very well the requirements for the SEM column to be used in spin-SEM. At a working distance of 8 mm (see below), a resolution of 7.5 nm is specified for a beam current of 1 nA at 3 keV primary energy. This current value fits well into the range that offers good working conditions, while the low primary energy is superior as it allows to operate close to the energy range where the SE yield becomes high.[18]

III. PRINCIPLES OF OPERATION

A. Standard spin-polarized LEED detector

In the LEED polarization detector, the diffraction of low-energy electrons at a W(100) single-crystal surface is used to measure the spin polarization. Almost 30 years ago, the spin-dependent scattering properties of the W(100) surface have been determined, both experimentally and theoretically.[19,20] The optimum working condition when utilizing the scattering at W(001) as a polarization detector was found using the (2,0) diffraction beams at 104.5 eV scattering energy. At this energy, a sensitivity $S = -0.27$ was obtained.[12,21]

In normal incidence, two orthogonal components of the spin polarization P of the incoming electrons can be determined from the normalized intensity differences (asymmetries) of two pair-wise opposed beams $\dot{N}_\uparrow$ and $\dot{N}_\downarrow$, or $\dot{N}_\rightarrow$ and $\dot{N}_\leftarrow$.

$$P_x = \frac{1}{S}\frac{\dot{N}_\uparrow - \dot{N}_\downarrow}{\dot{N}_\uparrow + \dot{N}_\downarrow}, \quad P_y = \frac{1}{S}\frac{\dot{N}_\rightarrow - \dot{N}_\leftarrow}{\dot{N}_\rightarrow + \dot{N}_\leftarrow}. \tag{1}$$

The total statistical error of a single polarization measurement using single-electron counting is governed by Poisson statistics. It can be expressed as[22]

$$\Delta P = 1/\sqrt{N S^2}. \tag{2}$$

For the LEED detector, $N = N(2,0) + N(\bar{2},0)$ is the total number of counts in two opposed beams for any fixed

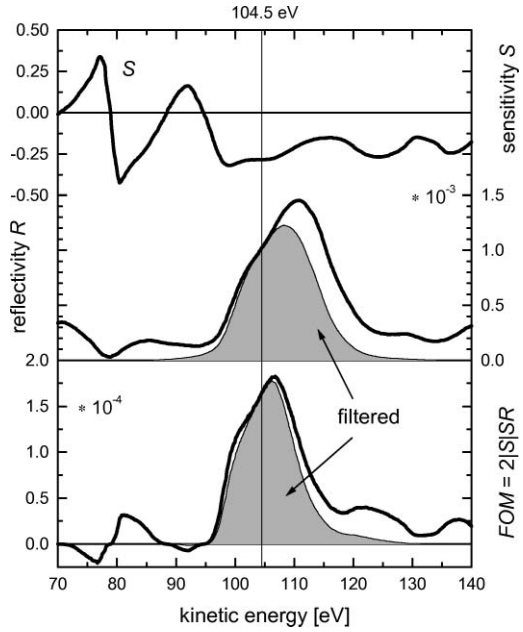

FIG. 3. Characteristics of spin-dependent scattering at the W(100) surface and the result of energy filtering in the detector. Energy-dependent detector spin-sensitivity S and reflectivity R data in normal incidence are reproduced from Ref. 12 for the (2,0) diffracted beams. The figure of merit in the lower panel is a measure of detector efficiency at the given energy. In order to illustrate the sign changes of the sensitivity, FOM has been redefined incorporating the sign of the sensitivity. The filtered curves indicate how the transmission and the resulting FOM are affected by the exit apertures of the scattering section of our detector.

acquisition time. As N is proportional to the reflectivity R, maximizing RS^2 minimizes ΔP. $2RS^2$, the so-called "Figure of Merit" (FOM), is, therefore, taken as measure for detector efficiency.[12] It allows for a direct comparison between different standard spin detectors, as it is derived from the statistical uncertainty of an individual polarization measurement. In calibration experiments for the LEED detector, it turned out that the maximum figure of merit of 1.6×10^{-4} is found at a kinetic energy of 104.5 eV,[12] using an energy spread of 1.5 eV and an angular spread of 0.5° at normal incidence. The reflectivity was determined to be $R = 0.0011$.

B. The LEED detector in SEMPA

If the LEED detector is used for polarization measurement in a SEM, such a simple relation is no longer meaningful. The reason for this is that three experimental conditions, which are more or less fulfilled in a typical spectroscopy experiment, are no longer valid for a SE polarization detector with high efficiency in spin-SEM application:

(a) The SEs cannot be considered monochromatic, compared to a scattering energy as low as 104.5 eV. SEs show a characteristic energy distribution, which is peaked around 2 eV, and extends up to a kinetic energy of 50 eV by definition. This distribution can be approximated by[23]

$$\frac{dn}{dE_{\mathrm{SE}}} \propto \frac{E_{\mathrm{SE}}}{(E_{\mathrm{SE}} + \phi_{\mathrm{W}})^4}, \tag{3}$$

with ϕ_{W} the work function as sole material parameter (see also Fig. 4). In this approximation, the peak position is given by $\phi_{\mathrm{W}}/3$.

(b) The spin polarization of the secondary electrons is energy dependent within the relevant energy range. For 3d-ferromagnets, the spin polarization of SEs at the lowest energy is strongly enhanced due to minority d-hole scattering on their way to the surface.[24] Only above 10–15 eV a constant value is obtained, which corresponds to the electron polarization of the occupied 3d-bands. Other classes of ferromagnetic materials can behave quite differently.

(c) The SE emission is not directional. Instead, it shows a cosine-type angular distribution, centered along the surface normal, with emission into the full half space.[23] This angular spread can be strongly reduced by an accelerating collection field, but the remaining angular divergence at the W crystal still has to be taken into account.

C. Strategy

In principle, it is possible to use an energy and angle resolving detector system, which selects electrons with a narrow energy and angle distribution out of the total SEs, while the majority of the SEs is discarded. The scattering intensity will be very low and measuring time has to be increased for statistical reasons. While such a detector can answer—according to Eq. (1)—the question for the exact spin polarization of the SE of a narrow energy interval at one spot, it cannot be practically used to visualize the lateral distribution of the polarization for typical imaging conditions with some 10000 pixels per image. As the focus is on the local orientation of the magnetization in the SEMPA investigation, the relative value of the polarization in different directions is of interest. Hence, it is recommendable to use a detector that accepts a wide range of SE energies and emission angles for the spin-polarization analysis in order to improve the signal to noise ratio by increasing intensity at the expense of polarization sensitivity. In addition, a large angular acceptance avoids possible image artifacts on polycrystalline samples with a pronounced angular dependence of spin polarization.

The experimental data of the double scattering experiment at W(100),[12] which are reproduced in the upper two panels of Fig. 3, reveal that both, sensitivity and reflectivity, vary strongly with energy around the optimum working point of 104.5 eV. Even a sign change of the sensitivity occurs some 9 eV below the optimum energy. Above 104.5 eV the reflectivity still increases up to 111 eV while the spin sensitivity gradually drops. These data indicate that the inclusion of electrons with wider energy spread will actually reduce the polarization sensitivity and, thus, the obtainable contrast. The lower panel of Fig. 3 shows the FOM for a nearly ideal detector with a small energy and angular spread like the one used in Ref. 12. We define the FOM as $FOM = 2\,|S|\,SR$. The latter formula differs from the conventional definition [Eq. (2)] to account for the effect of the sign changes of the sensitivity on the attainable detector properties when the energy spread is enlarged. The plot in Fig. 3 (lower panel) gives a hint to

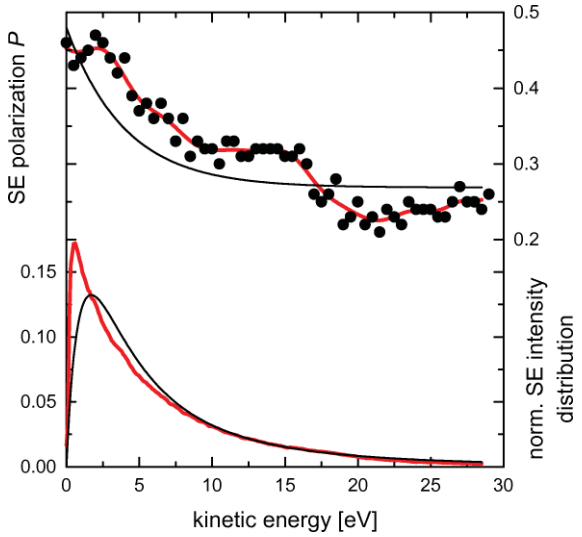

FIG. 4. (Color online) Spin-polarized secondary electron emission from iron. The upper panel shows the spectral distribution of the SE spin polarization. Two slightly different cases are shown: the dots are measured data for a clean Fe (110) single crystal, taken from Ref. 25. The thick (red) line gives a smoothed version of this data, which is used for the following calculations. The thinner (black) line approximates the SE polarization from a polycrystalline or amorphous iron sample (see text). The same color coding is used in the lower panel to describe the normalized energy distribution of the SE for the two cases. While the Fe(110) data are taken directly from the above-mentioned experiment, the distribution assumed for the polycrystalline case is calculated from Eq. (3) using a work function of 5 eV.

an operation window with an energy span fitting the SE energy distributions. The energy range between 99 and 112 eV with a slightly asymmetric peak in the FOM seems to be well suited.

The 13 eV energy interval is sufficient to analyze most of the SE with an energy distribution similarly to Eq. (3). It can be expected that tuning a detector to this working point will increase the performance of the spin-SEM. This qualitative argument, however, has to be quantified. The quantification is closely related to answers to the following questions:

(a) Which is the optimum scattering potential, i.e., the voltage to apply between sample and W crystal? In other words, how can the SE polarization and energy distributions be optimally mapped onto the distribution of the analyzer FOM?
(b) What asymmetry can be expected for a measurement at a given sample? This question asks for the obtainable image contrast in the polarization maps.
(c) What is the total detector performance for a given sample? This asks for the obtainable contrast/noise ratio per SE, which determines the quality of the local magnetization direction map calculated from the two polarization maps.
(d) Can angular- and/or energy-filtering apertures be beneficial to improve the detector performance?

In order to answer these questions, a numerical convolution of sample and detector properties in energy space will be carried out in the following.

D. Spin polarized secondary electron emission

At first, the exact polarization and energy distributions of the SE from a particular sample have to be known. We take the SE emission from Fe as the model system. Experimental data obtained at Fe(110) single-crystal surface are reproduced in Fig. 4.[25] The primary beam of 2 keV hits the surface at an angle of 60°, while the SE emission was investigated in normal emission. The polarization is highest ($P \sim 45\%$) at lowest energies and drops to about 25% for energies above 15 eV. Due to band-structure effects, a variety of substructures is superimposed onto the general trend.[26] The latter features depend on and vary with emission angle. Hence, when the angular acceptance is increased, a weighted average of all emission angles has to be used for maximum accuracy. In the following, we will just consider the normal emission data as prototype. In Fig. 4 the normalized SE distribution from Ref. 12 is plotted. The intensity is peaked at a very low energy of 0.6 eV. The angular acceptance is given as ±3° in the reference. Although energy and angular resolution are limited, we take this distribution as a good approximation of the true distribution.

As second sample we consider an amorphous/polycrystalline Fe sample because thin Fe films are frequently used as dusting layer for imaging in spin-SEM. Ultrathin polycrystalline Fe films are deposited onto samples that are otherwise not accessible for SEMPA, like oxides, nonitinerant ferromagnets, or samples with contaminated surfaces.[27] The decoration (or dusting) layer mirrors the magnetic structure of the underlying sample and provides the clean surface for spin-polarized SE emission, that is required for imaging.[7] Due to the lack of published energy-resolved polarization data from polycrystalline iron, measurements on the Fe-rich amorphous metallic glass $Fe_{80}B_{15}Si_4$ (Ref. 28) have been rescaled to describe pure Fe. The plot in Fig. 4 is the result of linearly scaling the metallic glass polarization data to match at higher energies (>20 eV) the expected Fe band polarization of 27%. The polarization distribution resulting from this procedure is in reasonable accordance with Monte Carlo simulation for noncrystalline iron.[29] Likewise, it fits more or less the general trend of the Fe(110) data, shown in the same panel. Numerically, we can represent the latter distribution, by $P_{SE}(E) = 0.27 + 0.21e^{-0.25E}$ for Fe.

The normalized intensity distribution for the amorphous Fe has been calculated from Eq. (3), assuming a work function of 5 eV for Fe (Fig. 2). This distribution is commonly believed to fit the general intensity distribution of SE in case of low angle and energy resolution.[23] The latter distribution has a peak at a significantly higher energy than the Fe(110) measurement; however, it coincides well with the experimental curve for Fe(110) above 10 eV.

E. Convolution of sample and scattering properties

As the most simple approach we first consider a detector without apertures, which detects scattered electrons from the (2,0) beams only. In that case, the transmission is solely determined by the reflectivity at the W crystal. For a monochromatic beam of polarization P and kinetic energy E being

scattered at the target, the observable intensity asymmetry A is given by [compare Eq. (1)]

$$A \equiv \frac{N_\uparrow - N_\downarrow}{N_\uparrow + N_\downarrow} = PS(E). \tag{4}$$

In order to facilitate the understanding, we will first consider a case where only electrons of two discrete scattering energies E_1 and E_2 were incident upon the crystal. The two electron beams are characterized by the relative frequencies n_1 and n_2 and the polarizations P_1 and P_2. The resulting asymmetry is then given by the weighted average of the individual asymmetries:

$$A = \frac{n_1 R(E_1)}{n_1 R(E_1) + n_2 R(E_2)} P_1 S(E_1) + \frac{n_2 R(E_2)}{n_1 R(E_1) + n_2 R(E_2)} P_2 S(E_2), \tag{5}$$

where weighting takes into account both, the initial frequency and the energy-dependent reflectivity at the crystal. If the incoming frequencies are normalized ($n_1 + n_2 = 1$), then the denominator gives directly the total transmission T, defined as the number of detectable electrons in each (2,0) LEED spot per incoming electron.

In SEMPA, we have to consider the continuous polarization and energy distributions of the incoming electrons, $P(E_{SE})$ and $n(E_{SE})$, the latter normalized by $\int_0^\infty n(E_{SE}) dE_{SE} = 1$. E_{SE} is the initial kinetic energy of the SE. To facilitate the notation further, we define $n(E_{SE} < 0) = 0$. The total apertureless transmission T can be calculated in analogy to the denominator of the simple two-energy case by integrating the product of energy distribution and associated reflectivity over the SE energy:

$$T(U) = \int_0^\infty n(E_{SE}) R(U + E_{SE}) dE_{SE} \equiv (\tilde{n} * R)(U). \tag{6}$$

Here $U = E - E_{SE}$ is the potential difference between sample and scattering crystal. By a simple substitution, it can be shown that this integral is mathematically equivalent to the convolution of a reversed energy distribution $\tilde{n}(E) = n(-E)$ with the reflectivity, as is given by the last part of Eq. (6). The numerator of Eq. (5) can be extended in a similar manner to continuous distributions by including the initial polarization and the spin sensitivity at the respective energies into the product in the integral. Thus, the resulting apertureless asymmetry is given by

$$A(U) = \frac{1}{T(U)} \times \int_0^\infty n(E_{SE}) P(E_{SE}) R(U + E_{SE}) S(U + E_{SE}) dE_{SE} \equiv \frac{1}{T(U)} \left(\tilde{n}\tilde{P} * RS\right)(U). \tag{7}$$

Again, this can be equivalently expressed in form of a convolution, if one uses the notation $\tilde{P}(E) = P(-E)$ for the energy-reversed polarization distribution. Note that U will be the only remaining free parameter in this simple model, if the four distributions used as input are known.

The quality of a SEMPA image, which is obtainable from a given total number of emitted SE, is entirely determined by knowing A and T. In analogy to the figure of merit of a spin detector for spectroscopy, as it is derived from the measurement uncertainty in Eq. (2), the quality parameter of a SEMPA measurement can be expressed as

$$Q(U) = 2A^2(U)T(U). \tag{8}$$

Q is no longer a pure detector property, as it also includes the information about the spin polarization and energy distribution of the SE from a particular sample. Only for a sample that caused 100% spin polarization at all relevant SE energies, Q would be equal to the energy-dependent FOM graphed in Fig. 3. For an Fe sample, Q is found to be roughly 1 order of magnitude smaller than the FOM.

Next, we apply these formulas to the two above discussed model distributions for Fe samples. As three of the input distributions are available as experimental data points only, both convolutions have been carried out by discrete summation, instead of using the integral form. Prior to summation, the distributions have been interpolated and discrete values generated on a common energy abscissa with 0.1 eV resolution. The results of the calculations are shown in Fig. 6 (dashed lines). The transmission curves for both cases are very similar. This is due to the normalization of the SE intensities and to the fact, that the reflectivity maximum is broader than the two energy distributions, so their differences are washed out by the convolution. Both have a maximum of 1.15‰ at around 106 eV, which means a 25% reduction compared to the

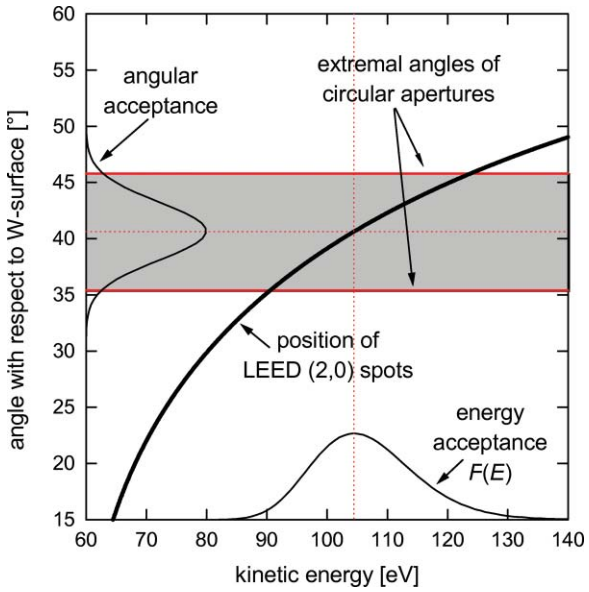

FIG. 5. (Color online) Illustration of the energy filtering properties of our LEED detector design. The calculated angular variation of the (2,0) LEED spots is shown as a function of kinetic energy together with the limiting angles at of the circular entrance apertures of the MCP section. The working point of the detector at 104.5 eV and the center position of the exit aperture at 40.64° are indicated as dotted lines. The Gaussian shaped angular acceptance on the left axis is transformed by the nonlinear energy dependency into the nonsymmetric energy acceptance shown on the bottom axis (both in arbitrary units and offset to the respective axes as zero).

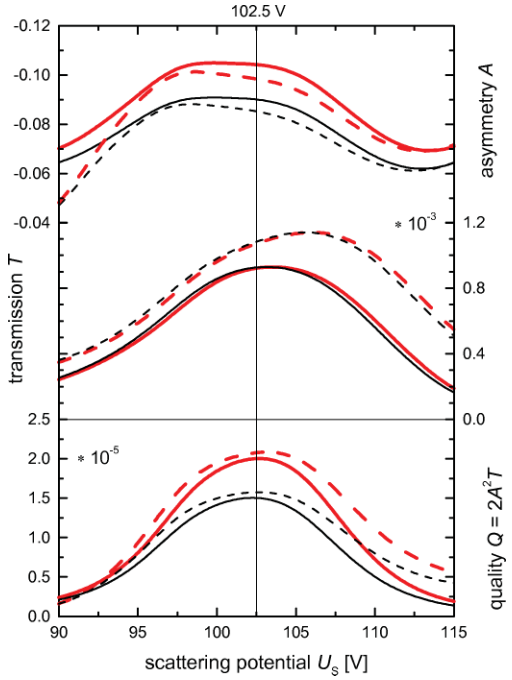

FIG. 6. (Color online) LEED detector output as function of the scattering potential U_S for SEs from Fe. The graphs show the asymmetry (top panel), transmission (middle panel), and quality (bottom panel), obtained by a convolution of sample and detector properties. Dashed lines show the results without filtering by a geometric exit aperture, while solid lines are calculated using the energy filter characteristic illustrated in Fig. 5. Due to its higher spectral weight at lowest energies, the single-crystalline model (thick red lines) achieves a higher asymmetry at the working point, compared to the polycrystalline model (thin black lines). The optimum voltage to be applied to the scattering crystal is 102.5 V, independent of the model, as can be seen from the quality graph.

maximum of the "monochromatic" reflectivity from Fig. 3. The optimum working point for SEMPA, however, is at the maximum in the Q graphs and turns out to be around 102.5 V for both sample systems. The latter is the best voltage to operate the detector. The transmission of 1.0‰ found at this voltage is equal to the one of a detector operating on monochromatic electrons at the respective working point

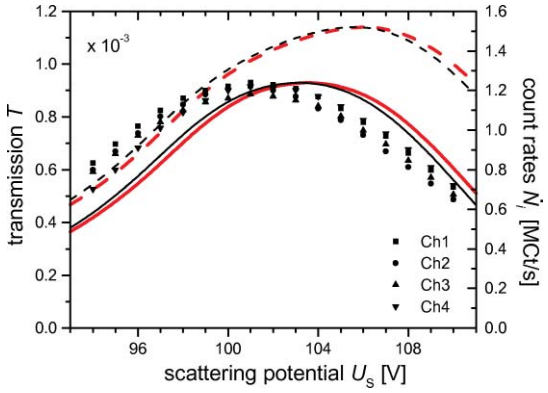

FIG. 7. (Color online) Comparison of the theoretical transmission curves from Fig. 6 (dashed and solid lines, as described there) with measured count rates (different style dots) as function of the scattering potential. Data points are recorded for the four channels Ch1-Ch4 simultaneously. The −2 eV shift of the measured data is attributed to hydrogen contamination of the detector crystal (see also text).

(104.5 eV). So from the apertureless approximation no losses are expected.

The asymmetry values are 10% for Fe(110) and 8.5% for the amorphous sample at the working point (Fig. 6). Monochromatic SE from Fe just above the work function barrier with an initial polarization of 48% would yield 13% asymmetry. The total spin sensitivity is, thus, clearly reduced by accepting a large number of less polarized SE. However, this is outweighed by the gain in transmission: Estimating the detector performance for monochromatized electrons gives $Q_{\mathrm{mono}} = 4 \times 10^{-6}$, by assuming a 1 eV wide energy acceptance window around the intensity maximum (12% of all emitted electrons). In comparison, the quantity Q is five times higher when all secondary electrons are accepted. Around the working point, the asymmetry in the nonfiltered case (Fig. 6) is depending on the potential. The asymmetry drops toward higher scattering potentials while it stays constant when reducing the potential. The falloff may cause artifacts when scanning or looking at inclined objects. We will show in Sec. III F, how an energy-filtering aperture can strongly reduce this effect.

The difference in asymmetry calculated for the two sample systems is also reflected in the Q graphs. Its main origin is the SE distribution, which is shifted for Fe(110) toward lower energies and thus enhances the weight of the strongly polarized electrons. If one calculates an average spin polarization of all SE for the two samples, weighting with the respective energy distributions, the Fe(110) model gives 39%, while the amorphous Fe gives 34%. This difference in average polarization is roughly proportional to the asymmetry difference found in the calculation.

F. Energy filtering and angular distribution

In order to calculate the properties of the detector precisely, the full trajectory of each SE has to be calculated, including the emission, the transmission to and scattering at the W crystal, and finally the transmission to the multiplier. In a simplified picture, three main effects have to be considered as function of initial emission angle and kinetic energy:

First, the spin sensitivity and reflectivity of the scattering at W(100) depend on the angle of the incoming electrons. The angle dependence has been experimentally studied for deviations from normal incidence of $\pm 1^\circ$ (Ref. 12) and up to $\pm 2^\circ$.[20] A slight variation of the energy-dependent sensitivity was observed, with an increase/decrease when tilting in the one/opposite direction. As long as the angular divergence of the incoming electrons stays within these limits, which can be ascertained by appropriate entrance apertures, these effects can be neglected.

Second, special features of the electron optics in front of the detector can cause losses. Possible origins are geometric apertures at the entrance or a limited strength of the collecting field. The latter are responsible for a loss of electrons at the fringes of the emission cone. Besides these limiting properties, which are directly correlated with details of the SE emission, a reduced transmission of the optics and/or retarding grids has to be considered. All these losses, together with re-

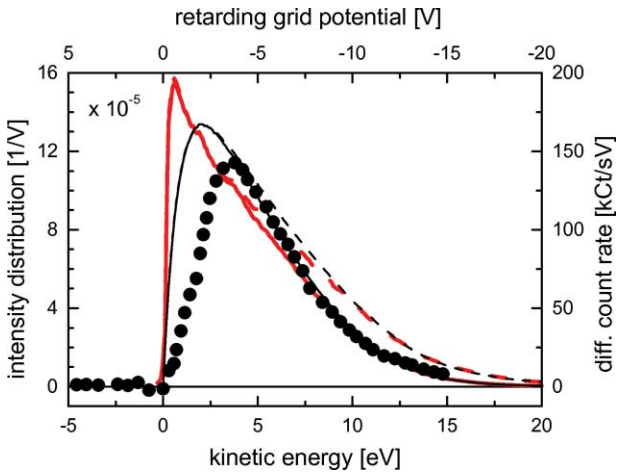

FIG. 8. (Color online) Energy distribution of the SE after scattering at W(001). Dots give the experimental results when the retarding grid voltage was varied between +5 and −15 V (top axis). The data shown are differentiated with respect to energy (right axis), to obtain the distribution. From the model, we obtain the dashed lines as energy distributions per channel and incoming electron (left and bottom axes; color/thickness designate the exact model used, as in the previous graphs). The energy filtering at the entrance apertures, which is included in the solid line calculations, is the reason for the gradual cutoff above 5 eV that is in perfect agreement with the measured data. At energies below 4 eV the grid transmission becomes less than unity, so the measured data falls off more rapidly. A scattering potential of 102.5 V has been used in the experiment and in the model.

duced detection efficiency of the electron counting facility, are put together into the global transmission figure. This figure is relevant for the final detector performance, and it can be determined experimentally from comparison with the ideal calculation, which will be finalized in the following. The abovementioned effects will not be modeled throughout the paper since they are largely independent of the polarization properties of sample or scattering crystal and have an effect on the experiment that is similar to a variation of the primary current of the SEM column.

Third, if an aperture is placed after the W crystal in front of the electron counters this exit aperture, in addition to angular filtering, will also have energy-filtering properties. The reason for this behavior is that the scattering angle is energy dependent. Thus, by an adequate shape and placement of apertures centered around the nominal direction of the (2,0) beams an energy window is defined. Only scattered electrons within a limited energy spread can be counted. Such an energy filter could improve the overall performance by rejecting electrons far away from the optimum energy that add only very little or even have a negative contribution to the detector performance. The implications of such an aperture will be modeled here, because it directly affects the polarization sensitivity.

The specific size and location of the exit apertures are taken from our detector design, which is described in detail in the preceding chapters. As indicated in Fig. 5, the four exit apertures are of circular shape and allow for a maximum angular divergence of $\pm 5^\circ$ when viewed from the center of the W crystal. Their positions are centered with respect to the outgoing (2,0) LEED spots of an optimum kinetic energy of 104.5 eV. The electron beam impinging on the W crystal has the same divergence of $\pm 5^\circ$, which is defined by the drift tube geometry (see Fig. 2). The same angle is also defined in the reverse beam direction by the lateral extension of the W-crystal, when it is viewed from the center positions of the exit apertures, so no electrons from further off angles can enter the apertures. Because of this consistent angular geometry, a very simple approximation is made to include the energy-filtering properties: The angular intensity distribution after the exit aperture is assumed to be of Gaussian shape with a width of $4\sigma = 10^\circ$, the full angular opening of the apertures. This shall account for the divergence of the incoming beam in two dimensions, as well as for the size and intensity distribution of the illuminated area on the crystal. The symmetric Gaussian shape of the angle acceptance (Fig. 5) can be converted into an energy acceptance utilizing the nonlinear energy dependence of the (2,0) scattering angle

$$\cos\vartheta(E) = \frac{2\lambda(E)}{a} = 7.757\sqrt{\frac{\mathrm{eV}}{E}}, \tag{9}$$

as illustrated in Fig. 5. The result is an asymmetric filter function

$$F(E) = \exp\left[-\frac{1}{2}\left(\frac{\vartheta(E)-\vartheta_0}{\sigma}\right)^2\right] = \exp\left[-2\left(\frac{\arccos(7.757\sqrt{\mathrm{eV}/E}) - 40.64^\circ}{5^\circ}\right)^2\right], \tag{10}$$

which falls off more rapidly to the low-energy side. The validity of this simplified filter model will be justified in Sec. IV by the good agreement to experimental findings**.** The filter function has been normalized to a peak value of 1, which by construction is located at $E_0 = 104.5$ eV. This accounts for the assumption that appropriate angular filtering has been performed by the drift tube before scattering, so all electrons scattered by the crystal with the exact energy E_0 can pass the exit apertures, irrespective of their initial angle. In order to include this filter characteristic into the detector model it has to be multiplied by the reflectivity R of the W crystal. The resulting filtered transmission FR is shown in the reflectivity graph of Fig. 3.

Looking at the polarization distribution, the asymmetric shape of the filter characteristics has the positive side effect to reduce the transmission for the electrons of reversed sensitivity at the lower energy side to at least 0.4, while maintaining reasonable transmission at the higher energy side where R is maximum and S is still acceptable. How well this chosen geometry matches to the scattering properties can be seen from the filtered FOM graph, which is given by $2|S|SFR$ and shown in the lower panel of Fig. 3. Under the assumption of unity transmission at E_0, most of the area with positive FOM around the working point can be made use of.

The consequences of the energy-filtering apertures for the performance of the detector are shown in Fig. 6 as continuous lines. All calculations for both sample systems have been repeated, with $R(E)$ replaced by $F(E)R(E)$ in Eqs. (6) and (7). A first observation is that the working point from the maxi-

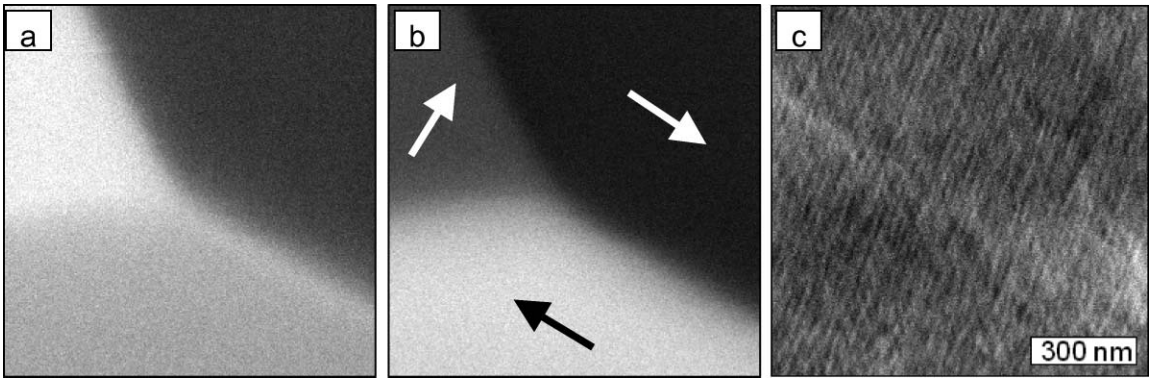

FIG. 9. SEMPA images from the Fe(100) whisker. The three images have been calculated from the simultaneously acquired intensity maps of the four detector channels. Panels (a) and (b) display the asymmetries corresponding to the y and x components of magnetization, respectively. Three magnetic domains are visible, with the magnetization (arrows) pointing along easy axes of magnetization. The surface Néel cap of the 180° wall is seen to extend as bright line from the center to the bottom right (a). Panel (c) gives the sum of all four channels and thus equals standard nonmagnetic SEM contrast. The lines running diagonally over the surface are grooves created by the low-angle sputter-cleaning process.

mum of the quality graphs is unchanged, which is due to the matched aperture position. Since the part of the electron energy distribution with reduced or even reversed asymmetry contributions have been filtered out, the expected asymmetry at the working point has risen to 10.5% for Fe(110) and 9% for the polycrystalline sample model compared to 9.8% and 8.5% without filtering. In addition, the dependency of the asymmetry on the scattering voltage is reduced, which should help to reduce image artifacts. On the other hand, the transmission with aperture is reduced by 14%. This is not fully compensated by the gain in asymmetry, so the quality is still slightly reduced (Fig. 6).

IV. SYSTEM PERFORMANCE

In this section, we conclude the predictions of the model and compare them to measured data. The ideal detector transmission T, as predicted by the model, is plotted in Fig. 7 as function of the scattering voltage U_S applied to the W(001) crystal. For comparison, the scattering intensities of the four diffraction channels, which have been obtained from an iron film, are plotted in the same graph (note the different ordinates). The experimental data are from a 2 nm thick *in situ* deposited Fe film on an oxidized Fe whisker. As the film exhibited a multitude of apparently random oriented domains within the field of view, no net magnetic contrast is observed in the area-integrated measurements. A primary beam of 1 nA/2 keV electrons was impinging at 64° onto the film. The upper curves in Fig. 7 (dashed lines) give the energy-dependent reflectivity of W(001) convoluted with the two SE energy distributions, i.e., the result of the simple model. Comparing the latter with the more precise model (solid lines), the effect of the limiting apertures becomes evident. The latter elements shift the maximum of transmission toward lower energies, where the spin sensitivity is higher (see the following discussion). The shape of the aperture filtered transmission

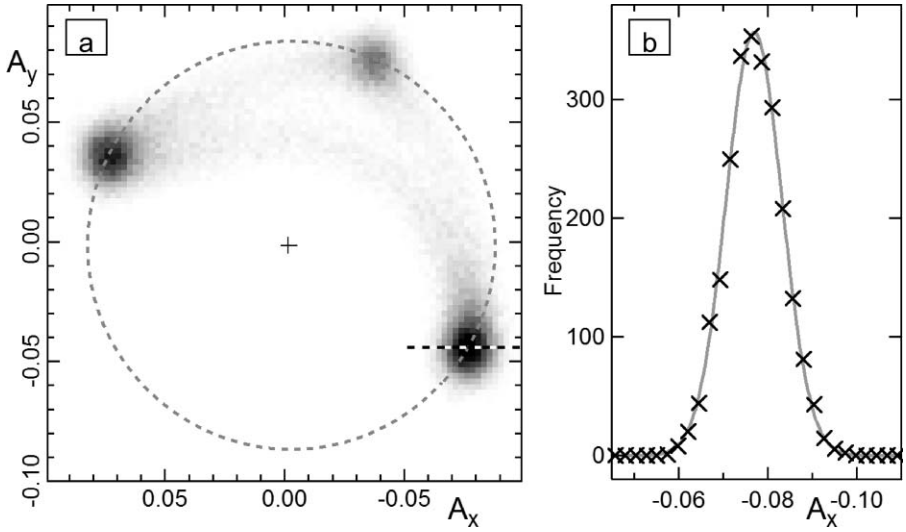

FIG. 10. Histogram (a) of the two-dimensional asymmetry distribution of the image in Fig. 9. The frequencies are counted per bin of 0.0025^2. Almost all of the intensity is concentrated in only three spots, which correspond to the three domains within the field of view. The radius of a circle drawn through the spots gives an asymmetry of 8.6%, which is in perfect agreement with our model calculation for polycrystalline iron. A profile across one of the spots in the histogram (dotted line) is shown in (b), together with a Gaussian fit yielding a standard deviation of 0.0065. Domain walls show up in the histogram as faint curved lines interconnecting the accumulation spots.

curve coincides very well with the observed single-channel transmission data. This demonstrates that the intended energy filtering can be obtained in a predictable way by limiting the diffracted beams by means of apertures. The energy shift of roughly −2 V in the experimental data can be explained by hydrogen contamination of the W surface. Such peak shifts as function of hydrogen coverage have been observed and interpreted in terms of different surface reconstructions that affect the W-interlayer spacing.[30] The dataset shown has been measured at a H_2 residual gas pressure of 2×10^{-9} mbar. Already some minutes after flash cleaning the peak position reaches a stable value although the surface is not yet hydrogen saturated. Under the improved vacuum conditions mentioned in the beginning, we find within 50 min a linear shift of the maximum of the distribution, starting from above 104 V to the shown value of 101 V. During this period, and at a fixed scattering voltage of 102.5 V, the measured image asymmetry remains stable within the span of 0.8–0.9. A detailed analysis of the effects of hydrogen adsorption on SEMPA measurements will be in the focus of a forthcoming paper.

In order to compare absolute numbers, one has to know the number of SE actually entering the detector, which is not easy to measure for experimental reasons. If one assumes an incoming SE current of 1 nA at the tungsten crystal, the calculation predicts a count rate of 5.5 MCt s^{-1}. This value is about five times larger than the count rates experimentally observed here. As the SE yield is not precisely known, we cannot calculate the exact SE current and count rates, the uncertainty in the yield is less than a factor 2. Thus, we might conclude that the reduction of the count rates is due to the reduced transmission and a reduction of the acceptance angle at the transfer optics. In addition, low-energy losses at the retarding grid have to be considered (see below), as well as the detection efficiency of the MCP stacks, which is typically of the order of 60%–70% at 700 eV kinetic energy. As those effects are not included in the model, we call that theoretical result the ideal transmission. Still, the obtained count rate, above 10^6 per second and channel, allows for taking quick overview images from iron samples within less than a minute, or taking high-quality images within 5–10 min.

An important crosscheck of the detector performance, especially concerning the cleanliness and quality of the W crystal, can be experimentally performed by varying the retarding grid voltage while keeping the scattering potential fixed. In Fig. 8 the energy derivative of the measured count rates versus retarding grid potential is plotted. The plot looks (and actually should look) very similar to the principal SE intensity distribution. The dashed line in the plot is the SE intensity distribution convolved with the W(001) reflectivity, while the solid curve is the same distribution corrected for the influence of the energy-filtering aperture. Again, the results of the experiment and the latter model curve fit very well. From the plot, the effect of the aperture becomes evident. Electrons above 10 eV, which have lower polarization, are suppressed. The noticeable reduction of transmission between 0 and 3 eV is a common detriment of a retarding grid setup.[31] From a higher-energy fit of the measured transmission to the model transmission a total grid transmission of 80% can be estimated. In the present detector, this breakdown of low-energy transmission at the retarding grid will strongly reduce the higher image asymmetry of the single crystalline Fe sample predicted in the model calculation. The total detector intensity distribution found here is roughly 20 times wider than the distribution that has been calculated for a standard LEED operating at high resolution.[21] It is still twice the width found in the same study for the optics running in a high-transmission mode.

The latter experiment, measuring the energy distribution via modulation of the retarding grid potential, has turned out to be a very useful tool for checking the operation of the LEED detector. For instance, if the surface of the W(001) crystal is not well prepared, there will be a noticeable diffuse background at positive retarding grid voltages in the differentiated signal. Any charging at the sample can immediately be noticed from a peak shift in this distribution.

A. Image contrast and noise

So far, we have only shown energy-resolved experimental data without considering magnetic properties. In order to characterize our detector and to test the model calculation on sensitivity, the analysis of magnetic images is required. Figure 9 shows the domain image of a detail at the surface of an Fe(100) oriented single crystal (whisker)**.** The whisker is several 100 μm in profile, about 1 cm long, running at an angle of 30° with respect to the image frame. We have sputtered the whisker by extended 1 keV Ar ion bombardment to obtain a clean ferromagnetic surface. The three images of Fig. 9 have been calculated from the four simultaneously acquired intensity maps of the independent detector channels. Panels (a) and (b) display the local asymmetry corresponding to the y and x components of magnetization. The magnetic structure of an unstrained (100) oriented iron whisker is governed by the cubic volume anisotropy with easy axes along ⟨100⟩ directions in the surface plane. Therefore, aside from domain walls, only four in-plane directions of magnetization exist at the (100) surface and no out-of-plane component is expected. Of these four directions, only three magnetic domains are visible in the image. They form two 90° walls oriented at 45° to the easy axes. The surface Néel cap of a 180° wall[1] is seen to extend as white line from the center to the lower right. Panel (c) gives the sum of all four channels and, thus, the standard nonmagnetic SEM contrast. The lines running diagonally over the surface are grooves originating from the low-angle sputter-cleaning process. This set of images demonstrate the perfect separation of magnetic and nonmagnetic informations within one dataset that is possible with a well-balanced detector on a nearly flat surface. For strongly corrugated objects, however, topographic effects can lead to artifacts in the magnetic contrast. The image has been acquired with a primary beam of 3 nA at 10 keV. It consists of 64 kpixels and has a total size of 1 μm^2. The dwell time per pixel was 5 ms, yielding roughly 13 kCt per pixel and per channel, and a total acquisition time of 5.5 min.

In order to analyze such an image quantitatively, the statistical distribution of all measured asymmetry (x,y) doublets within the image has to be evaluated.[32] This is done using the two-dimensional asymmetry histogram given in Fig. 10,

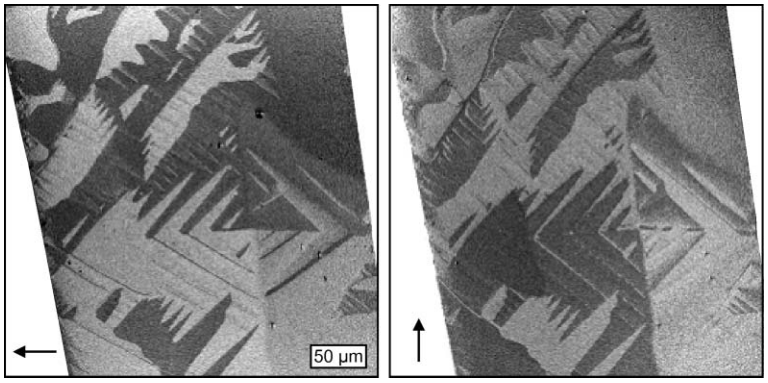

FIG. 11. Overview asymmetry images showing the full width of a second, less perfectly grown, Fe whisker. The observed fir-tree domain pattern indicates that its surfaces are only vicinal to {001} and that several twin boundaries are present. There is almost no shift in the sensitivity or the experimental asymmetry over the entire field of view of 350 μm.

which has been calculated from the data of Figs. 9(a) and 9(b). Three dark spots visible in the histogram indicate the presence of three predominant asymmetry doublets in the data. They can, thus, be identified with the three magnetic domains of the image. The fourth possible domain orientation, which is absent from the image, would complete the isosceles triangle formed by the three spots into a square. The center of this square (marked by a cross) corresponds to zero spin polarization and, thus, gives the experimental asymmetry of the detector for this measurement. From the radius of a circle that is centered on this point, and passes through the accumulation points, the magnitude of the image asymmetry can be determined. We find a value of 8.6%, which is only slightly less than the 9% predicted from our model calculation for polycrystalline iron (see upper panel of Fig. 6). Because the whisker was not annealed after sputtering, the surface layers defining the spin polarization will be disordered, so this comparison is reasonable. The image contrast, by common definition the difference of the darkest and the brightest areas of an image normalized by the average intensity, is twice this value and thus 17.2%. A second quantitative measure to be extracted from the histogram is the noise of the image. It is given by the uncertainty of the asymmetry measurement due to limited statistics and can be extracted from the profile of an accumulation point. A Gaussian fit to the line profile across one of the spots of Fig. 10 yields a standard deviation of $\sigma = 0.0065$, which conforms to the error of $1/\sqrt{26\,000} = 0.0062$ for the Poisson statistics of a single measurement.The image quality can be quantified by the contrast to noise ratio (CNR), which is about 26.5 for the image shown. It scales with $\sqrt{Q\Delta t}$, where Δt is the acquisition time per pixel and Q the quality of the detector.

From such experimental data, a direct comparison of different SEMPA systems is possible. For a system based on the LEDS detector, a set of data for identical conditions (10 keV primary electrons incident on a clean iron surface) have been published.[33] Unguris *et al.* define a total quality parameter $C \equiv 4\Delta t\, I_P/(\mathrm{CNR})^2$ that includes the SE emissivity and links the image contrast directly to the number of incoming primary electrons per pixel. We find $C = 9 \times 10^{-14}$As in comparison to $C = 2 \times 10^{-13}$As for the LEDS detector. This means that at the same primary electron current I_P less than half the time is needed with the new LEED system to record an image of identical CNR. This advantage is by a significant part due to a larger sample tilt and, therefore, higher SE yield in our setup. In addition, the higher S of the LEED detector strongly reduces the susceptibility to instrumental asymmetries. Compared to our own previous LEED based instrument,[14] roughly 1 order of magnitude reduction of acquisition time is gained by the new setup.

Beyond detector quality, further quantitative information about the magnetization pattern can be extracted from the histogram: The possibility to determine the in-plane angle of the local magnetization with small uncertainty [$\arctan(\pm 0.0065/0.086) \cong \pm 4^\circ$] has been used to investigate fine magnetization details of artificially patterned nanostructures, which reveal information about dipolar coupling and edge roughness.[34] By analyzing the radius between the center and each asymmetry point in the histogram, the magnitude of the projected magnetization onto the detector plane can be determined. This has been applied together with the angular information to the analysis of the complex three-dimensional domain structure of the canted phase of ultrathin films close to spin reorientation transition.[35] An additional feature of the detector is demonstrated in Fig. 11. Due to the well-defined divergence of the beam in the drift tube, it is easy to find lens settings that allow for a wide field of view, while a homogeneous instrumental asymmetry and homogeneous spin sensitivity are maintained. The example given shows the full lateral extent of a less perfectly grown Fe whisker. The nonideal structure can be deduced from the observed fir-tree domain patterns, which are typical for vicinal {001} surfaces. Several changes of pattern orientation, together with the sum image (not shown), hint at the presence of twin boundaries within the image. Image sizes of about $(500\ \mu\mathrm{m})^2$ are feasible. In the example given, the local magnetic structure can hardly be understood without such an overview image—a fact that equally well holds, e.g., for the study of coupling in arrays of magnetic nanostructures.

ACKNOWLEDGMENTS

Financial support by the German Federal Ministry of Education and Research has been granted under BMBF

13N7484. We acknowledge additional funding by DFG within SFB668. We thank F. Lofink for critical reading and discussions.

[1]H. P. Oepen and J. Kirschner, Phys. Rev. Lett. **62** (7), 819 (1989).
[2]M. R. Scheinfein, J. Unguris, R. J. Celotta, and D. T. Pierce, Phys. Rev. Lett. **63** (6), 668 (1989).
[3]H. P. Oepen, J. Magn. Magn. Mater. **93**, 116 (1991).
[4]J. Unguris, R. J. Celotta, and D. T. Pierce, Phys. Rev. Lett. **67** (1), 140 (1991); H. Hopster, Phys. Rev. Lett. **83** (6), 1227 (1999).
[5]M. Konoto, T. Kohashi, K. Koike, T. Arima, Y. Kaneko, T. Kimura, and Y. Tokura, Phys. Rev. Lett. **93** (10), 107201 (2004); Phys. Rev. B **71**, 184441 (2005).
[6]R. Allenspach and A. Bischof, Phys. Rev. Lett. **69** (23), 3385 (1992); R. Allenspach, M. Stampanoni, and A. Bischof, Phys. Rev. Lett. **65** (26), 3344 (1990); M. Speckmann, H. P. Oepen, and H. Ibach, Phys. Rev. Lett. **75** (10), 2035 (1995).
[7]T. VanZandt, R. Browning, and M. Landolt, J. Appl. Phys. **69** (3), 1564 (1991).
[8]T. Kohashi and K. Koike, Jpn. J. Appl. Phys. **40**, L1264 (2001); T. Kohashi, M. Konoto, and K. Koike, J. Electron Microsc. **59** (1), 43 (2010).
[9]Developed in cooperation with Carl Zeiss NTS GmbH, CEOS GmbH, and Omicron. NanoTechnology GmbH.
[10]K. Koike and K. Hayakawa, Jpn. J. Appl. Phys. **23** (3), L187 (1984); R. Allenspach, J. Magn. Magn. Mater. **129** (2–3), 160 (1994).
[11]M. R. Scheinfein, D. T. Pierce, J. Unguris, J. J. McClelland, R. J. Celotta, and M. H. Kelley, Rev. Sci. Instrum. **60** (1), 1 (1989).
[12]J. Kirschner, *Polarized Electrons at Surfaces* (Springer-Verlag, Berlin, 1985).
[13]H. P. Oepen and J. Kirschner, J. Phys. (Paris) **49** C-8 (Colloque C8), 1853 (1988).
[14]H. P. Oepen and J. Kirschner, Scanning Microsc. **5** (1), 1 (1991).
[15]M. R. Scheinfein, J. Unguris, M. H. Kelley, D. T. Pierce, and R. J. Celotta, Rev. Sci. Instrum. **61** (10), 2501 (1990).
[16]R. Bertacco, M. Merano, and F. Ciccacci, Appl. Phys. Lett. **72** (16), 2050 (1998); A. Winkelmann, D. Hartung, H. Engelhard, C. T. Chiang, and J. Kirschner, Rev. Sci. Instrum. **79** (8), 083303 (2008); T. Okuda, Y. Takeichi, Y. Maeda, A. Harasawa, I. Matsuda, T. Kinoshita, and A. Kakizaki, *ibid.* **79** (12), 123117 (2008).
[17]C. Jozwiak, J. Graf, G. Lebedev, N. Andresen, A. K. Schmid, A. V. Fedorov, F. El Gabaly, W. Wan, A. Lanzara, and Z. Hussain, Rev. Sci. Instrum. **81** (5), 053904 (2010).
[18]H. P. Oepen and H. Hopster, in *Magnetic Microscopy of Nanostructures*, edited by H. Hopster and H. P. Oepen (Springer, Berlin, 2005), pp. 137.
[19]J. Kirschner and R. Feder, Phys. Rev. Lett. **42** (15), 1008 (1979); R. Feder and J. Kirschner, Surf. Sci. **103** (1), 75 (1981).
[20]G. C. Wang, R. J. Celotta, and D. T. Pierce, Phys. Rev. B **23** (4), 1761 (1981).
[21]D. Yu, C. Math, M. Meier, M. Escher, G. Rangelov, and M. Donath, Surf. Sci. **601** (24), 5803 (2007).
[22]J. Kessler, *Polarized Electrons*, 2nd ed. (Springer-Verlag, Berlin, 1985).
[23]L. Reimer, *Scanning Electron Microscopy: Physics of Image Formation and Microanalysis*, 2nd ed. (Springer-Verlag, Berlin, 1998).
[24]G. Schönhense and H. C. Siegmann, Ann. Phys. **2** (5), 465 (1993).
[25]J. Kirschner and K. Koike, Surf. Sci. **273** (1–2), 147 (1992).
[26]H. Hopster, R. Raue, E. Kisker, G. Güntherodt, and M. Campagna, Phys. Rev. Lett. **50** (1), 70 (1983); M. S. Hammond, G. Fahsold, and J. Kirschner, Phys. Rev. B **45** (11), 6131 (1992).
[27]H. Hopster and H. P. Oepen, *Magnetic Microscopy of Nanostructures* (Springer, Berlin, 2005), pp. 313.
[28]H. Hopster, Phys. Rev. B **36** (4), 2325 (1987).
[29]M. Yasuda, K. Tamura, H. Kawata, and K. Murata, J. Phys. D **34** (13), 1955 (2001).
[30]D. A. King and G. Thomas, Surf. Sci. **92** (1), 201 (1980); R. A. Barker and P. J. Estrup, J. Chem. Phys. **74** (2), 1442 (1981).
[31]D. A. Huchital and J. D. Rigden, J. Appl. Phys. **43** (5), 2291 (1972).
[32]R. Frömter, C. Menk, H. Stillrich, and H. P. Oepen, Vacuum **82** (4), 395 (2007).
[33]J. Unguris, in *Experimental Methods in the Physical Sciences*, edited by Marc De Graef and Yimei Zhu (Academic, San Diego, 2001), Vol. 36, pp. 295.
[34]S. Hankemeier, R. Frömter, N. Mikuszeit, D. Stickler, H. Stillrich, S. Pütter, E. Y. Vedmedenko, and H. P. Oepen, Phys. Rev. Lett. **103** (14), 147204 (2009).
[35]R. Frömter, H. Stillrich, C. Menk, and H. P. Oepen, Phys. Rev. Lett. **100** (20), 207202 (2008).